Chinese Chemical Letters 37 (2026) 112508

Contents lists available at ScienceDirect

Chinese Chemical Letters

journal homepage: www.elsevier.com/locate/cclet

Enlarged Fe-O covalency enabled by Mo incorporation for water remediation

Jiaqi Wu[a], Fengze Zhuang[a], Yuqiu Xie[a], Yue Chen[a], Xiaofei Zeng[a], Liang Chen[a], Bocheng Qiu[b,*], Qiaohong Zhu[a,*], Mingyang Xing[a,c,d,**]

[a] Key Laboratory of Organosilicon Chemistry and Material Technology, Ministry of Education, Zhejiang Key Laboratory of Organosilicon Material Technology, College of Material, Chemistry and Chemical Engineering, Hangzhou Normal University, Hangzhou 311121, China
[b] Department of Chemistry, College of Sciences, Nanjing Agricultural University, Nanjing 210095, China
[c] Key Laboratory for Advanced Materials and Joint International Research Laboratory of Precision Chemistry and Molecular Engineering, Feringa Nobel Prize Scientist Joint Research Center, School of Chemistry and Molecular Engineering, East China University of Science and Technology, Shanghai 200237, China
[d] Shanghai Engineering Research Center for Multimedia Environmental Catalysis and Resource Utilization, East China University of Science and Technology, Shanghai 200237, China

ARTICLE INFO

Article history:
Received 24 September 2025
Revised 12 December 2025
Accepted 5 February 2026
Available online 6 February 2026

Keywords:
Charge redistribution
Fe-O covalency
Metal redox cycling
Fenton-like reaction
Antibiotic wastewater removal

ABSTRACT

The worldwide utilization of antibiotics and the generation of antibiotic-resistant bacteria necessitate the development of alternative wastewater treatment strategies, in which the cycling of metallic ions and the precise modulation of Fe active sites remain critically important factors to be concerned. In this work, Mo incorporation is strategically employed to modulate Fe-O covalency through charge redistribution driven by strong Fe-Mo interactions over graphite carbon ring/CN (CCN). This design achieves an exceptional degradation rate constant, which arises from synergistic Fe/Mo catalytic-co-catalytic interactions that facilitate sustainable metal redox cycling, enhance bonding orbital overlap, and optimize surface adsorption characteristics. The Mo-modified catalyst (FeMoCCN) exhibits a greater contribution to bonding orbitals compared to the singly Fe-doped counterpart (FeCCN). The introduction of Mo enhances Fe-O covalency, thereby facilitating electron transfer for peroxymonosulfate (PMS) activation and subsequent degradation processes. Remarkably, complete electron transfer is achieved through the Fe^{2+}/Fe^{3+}, Mo^{6+}/Mo^{4+}, Fe^{3+}/Mo^{4+} redox couples, further implying the robust adaptability of this Fenton-like system for antibiotic degradation while providing mechanistic insights into the synergistic effects between light irradiation, oxidant activation, and bimetallic doping modulation in advanced wastewater treatment.

© 2026 Published by Elsevier B.V. on behalf of Chinese Chemical Society and Institute of Materia Medica, Chinese Academy of Medical Sciences.

Fenton-like water treatment technology has been developed as an imperative candidate for antibiotic wastewater control, thus avoiding the accumulation of antibiotics in ecological environment and living organism [1–3]. Notably, sulfate radical ($SO_4^{\bullet-}$)-based advanced oxidation processes (SR-AOPs) among various Fenton-like reactions, in which peroxymonosulfate (PMS) or persulfate (PS) are activated accompanied with the broken of peroxo bonds (O–O), have been proven with outstanding efficiency and sustainable capacity [4,5]. Furthermore, there also exist the non-radical pathways in SR-AOPs, *e.g.*, the formation of high valent iron-oxo species like $\equiv Fe^{IV}=O/\equiv Fe^{V}=O$, and the existence of singlet oxygen ($^1O_2$), which have been widely investigated owing to their strong oxidation capability and compelling stability [6–9]. Nevertheless, the circulation of transition metallic ions involved in PMS activation remains unsatisfied, and the dissolution of metal ions is endowed with vital importance for practical applications [10–12]. At this juncture, light-driven PMS activation using heterogeneous photocatalysts has riveted the attention of researchers, in which the photo-generated electrons are advantageous for PMS activation as well as metal ions redox cycling [13]. However, in-deep investigation over electronic structure modulation and reaction mechanism is still a critical and complex issue, which need to be further explored.

Notwithstanding, the pivotal role of metal active sites is non-negligible for PMS activation, attributed to its tunable electronic structures and highly efficient performance. Accordingly, PMS activation using metal-based catalysts is demonstrated advantageous,

* Corresponding authors.
** Corresponding author at: Key Laboratory for Advanced Materials and Joint International Research Laboratory of Precision Chemistry and Molecular Engineering, Feringa Nobel Prize Scientist Joint Research Center, School of Chemistry and Molecular Engineering, East China University of Science and Technology, Shanghai 200237, China.
E-mail addresses: bochengqiu@njau.edu.cn (B. Qiu), zhuqh@hznu.edu.cn (Q. Zhu), mingyangxing@ecust.edu.cn (M. Xing).

https://doi.org/10.1016/j.cclet.2026.112508
1001-8417/© 2026 Published by Elsevier B.V. on behalf of Chinese Chemical Society and Institute of Materia Medica, Chinese Academy of Medical Sciences.

however, the sluggish metal redox cycling remains the bottleneck for the practical application [14,15]. It is noteworthy that diverse strategies have been utilized to stabilize metal elements in the supporting base for selective oxidation through PMS activation, like the formation of M-N_x bonds between metal with the supporting base to stabilize and disperse metal atoms [16]. Taking an example, a series of boron nitride-based single-atom catalysts (Co, Fe, Cu, Ni and Mn) with M-N_3 sites was explored by Zhen *et al.* through the control of vacancy using Zn salt and coordination anchoring pathway, thus realizing high selectivity of $^1O_2$ and catalytic performance [6]. In Fenton-like systems, studies on Fe-activated PMS have revealed the advantages of co-catalytic sites (such as Mo sites). The asymmetric charge distribution created by dual-atom catalysts can modulate the electron density of Fe sites through metal-metal interaction, thereby influencing the adsorption and activation capabilities of material [17]. Notably, the electronic structure of metal active sites is vital for the redox reaction, in which bimetallic-doping strategy can be utilized to realize charge distribution around metal central sites, thus affecting the metal-O covalency for electron transfer capacity and surface adsorption/activation for further degradation.

Herein, Mo is introduced to modulate Fe-O covalency with charge redistribution over graphite carbon ring/CN (CCN) *via* tight Fe-Mo interactions and the synthesized FeMoCCN was utilized for antibiotic wastewater remediation. Experimental characterizations have been probed to detect the existing reaction active species in the free radical and non-radical pathway of the system, and a higher selectivity of singlet oxygen was detected in the synergistic system. Combined with density functional theory (DFT) calculations, the contribution of FeMoCCN to the bonding orbitals is higher than that of FeCCN, and the Fe-O covalency is obviously enlarged with Mo incorporation, which is beneficial for electrons transfer for further PMS activation and wastewater removal. Additionally, a sustainable electron transformation between Fe and Mo atoms is realized, attributed to the synergistic Fe/Mo catalytic-co-catalytic interactions as well as continuous generation and transfer of electrons upon light irradiation, thus providing novel Fenton-like catalytic systems for green wastewater removal.

The crystal structures of catalysts were explored through X-ray diffraction (XRD) patterns, as displayed in Fig. 1a. Obviously, two distinct peaks at 13.1° and 27.4° were observed for CCN, corresponding to the in-plane stacking (100) and interlayer stacking (002) of carbon nitride. The decreased peak intensity compared to CN can be attributed to the conjugation of carbon nitride with the carbon ring, which might break part of the C–N arrangement (Fig. S1 in Supporting information) [18]. Moreover, the reduced intensity and broadened peaks of MoCCN and FeMoCCN relative to CCN might result from the partial entry of Mo and Fe into the channels, as well as a decrease in the interlayer stacking distance of the heptazine rings. Of note, the new peak that appears at 1731 cm^{-1} in Fourier transform infrared (FTIR) spectrum is assigned to the C=O bond, which can be attributed to the introduction of glucose and its connection with the terminal amino groups of carbon nitride (Figs. S2-S4 in Supporting information) [19]. The morphology of the catalysts is explored using transmission electron microscopy (TEM) and high-resolution transmission electron microscopy (HRTEM). Normally, two-dimensional layered morphology of FeMoCCN can be observed, similar with that of CCN, MoCCN, and FeCCN, manifesting that the introduction of Fe or Mo does not disrupt the integrity of the structure (Fig. 1b and Fig. S5 in Supporting information). Additionally, energy-dispersive X-ray spectroscopic elemental mapping indicates the uniform distribution of C, N, Fe, and Mo elements, suggesting that the successful introduction of Fe and Mo into CCN, further illustrating the successful synthesis of FeMoCCN (Fig. S6 in Supporting information).

Subsequently, the chemical properties and composition of the catalysts are identified by X-ray photoelectron spectroscopy (XPS). As shown in Fig. S7 (Supporting information), the peaks are divided into three characteristic peaks at 284.8, 286.3 and 288.3 eV, corresponding to C-C/C=C, C-NH_x and N-C=N, respectively. The N-C=N peak positions of MoCCN, FeCCN, and FeMoCCN show positive shifts, attributed to the fact that metal doping might affect the carbonization degree of catalysts [20]. Besides, there exist three peaks at 398.6, 400.0, and 401.1 eV for CCN in N 1s spectra, which are assigned to pyridinic N (C-N=C), pyrrolic N (N-$(C)_3$), and graphitic N (C-NH_x), respectively (Fig. S8 in Supporting information). Intriguingly, it is observed that the characteristic peaks of pyridinic N in MoCCN, FeCCN, and FeMoCCN all shift to higher values, implying the reduction in the electron density around pyridinic N atoms. This observation is attributed to the fact that the sp^2 hybridized N atoms can provide unpaired lone pair electrons to the molecular orbitals of the metal elements along with the formation of metal-N bonds [9]. Additionally, two new peaks appear at the location of 397.3 and 399.6 eV, which are attached to the Mo-N and Fe-N bonds, respectively, further confirming the successful introduction of Fe and Mo elements [21]. Furthermore, the peaks located at 711.6 and 725.4 eV in the Fe 2p XPS spectra are attributed to Fe $2p_{3/2}$ and Fe $2p_{1/2}$, respectively, while the peaks at 719.8 and 733.0 eV reflect the satellite peaks (Fig. 1c). Therefore, two oxidation states of Fe^{2+} and Fe^{3+} both exist, while no significant peak is observed for Fe^0, indirectly suggesting that iron may be coordinated and bonded with the Mo, C, and N elements. Moreover, the content of Fe^{2+} increased with the Mo addition from 39.0 % in FeCCN to 59.7 % in FeMoCCN, and the ratio of Fe^{2+}/Fe^{3+} has increased by 1.3, demonstrating that the introduction of Mo might contribute to the electron distribution adjustment around Fe atoms, confirmed by the negative peak shifts and increased electron density of Fe elements over FeMoCCN as compared to FeCCN [4]. Besides, as manifested in Fig. 1d, the binding energy at 229.0, 232.2, and 235.2 eV are attributed to Mo^{4+} $3d_{5/2}$, Mo^{4+} $3d_{3/2}$, and Mo^{6+} $3d_{3/2}$, respectively. The significant presence of Mo^{4+} with certain reducing capacity is advantageous for electron transfer, especially facilitating the conversion of Fe^{3+} to Fe^{2+}. Most importantly, the positive shift of all the peaks of FeMoCCN might be a result of the formation of Mo-N bonds and the electron distribution adjustment inside the structure [22].

Additionally, the valence and bonding states of Fe and Mo in FeMoCCN were further revealed by X-ray absorption near-edge structure (XANES) and extended X-ray absorption fine structure (EXAFS). Comparing the XANES data of different states of Fe (FeMoCCN, Fe foil, Fe_2O_3, FeO, FePc) in Fig. 1e, it can be seen that the absorption edge energy of FeMoCCN emerges between FeO and Fe_2O_3, and the linear relationship of the absorption edge obtained for Fe is 2.4 (Fig. 1f), indicating that Fe displays an intermediate valence state, fluctuating between +2 and +3. This is likely ascribed to the influence of C ring and Mo on the electronic state and coordination environment around Fe. Meanwhile, the R-space EXAFS spectra show a significant peak at 1.5 Å, which is the same as the Fe-N peak position in FePc, and no obvious Fe-Fe and Fe-O coordination peaks are observed (Fig. 1g) [23]. Furthermore, combining the fitting curves and their related parameters, it is discovered that the fitting curve matches the Fe-N model, with a coordination number of 4 and a bond length of around 2.05 Å, revealing that Fe in FeMoCCN mainly exists in the form of Fe-N_4 coordination (Fig. 1h and Table S1 in Supporting information). Subsequently, by comparing positions of Fe-Fe (7.8 $Å^{-1}$), Fe-O (4.8 $Å^{-1}$), and Fe-N (5.0 $Å^{-1}$) in the wavelet transform (WT) EXAFS of Fe foil, Fe_2O_3, and FePc, it is found that FeMoCCN only exhibits a maximum density at 5.0 $Å^{-1}$, corresponding to Fe-N, further confirming the abundance of metal-N bonds in this catalyst (Figs. 1m and

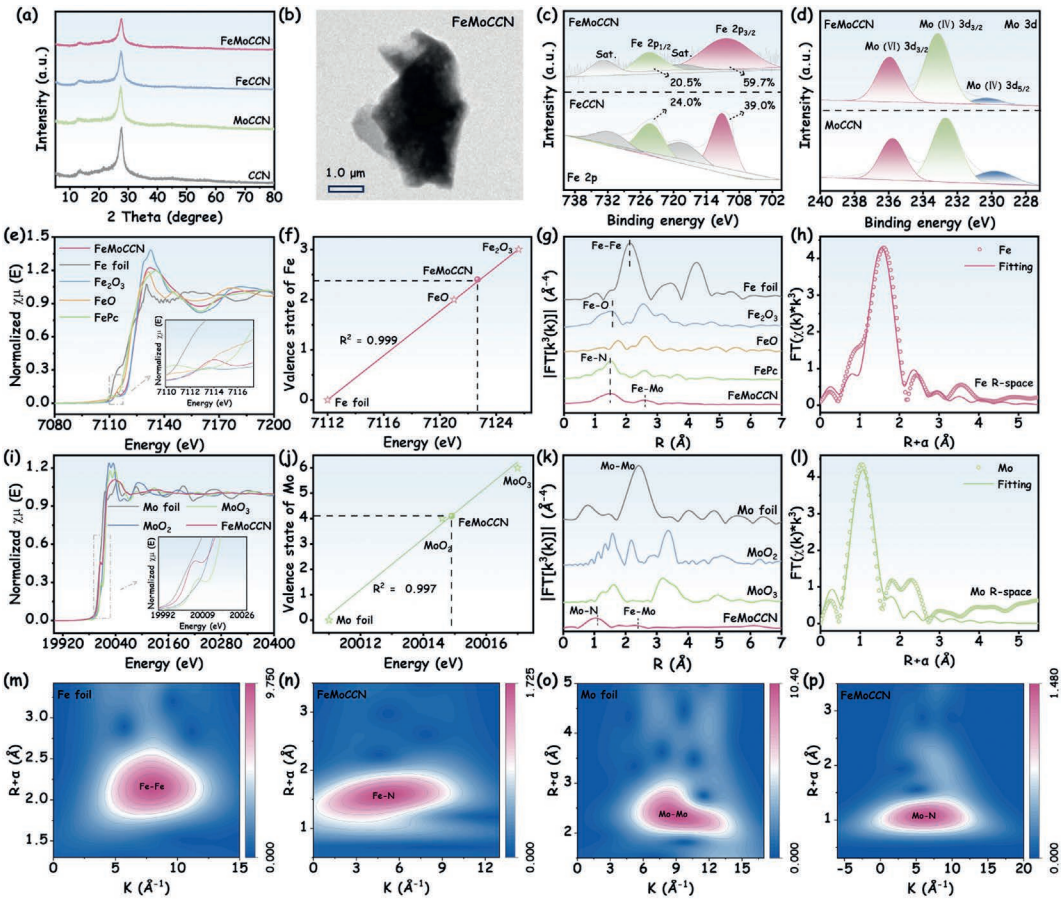


Fig. 1. (a) XRD patterns of samples. (b) TEM image of FeMoCCN. XPS analysis: (c) Fe 2p spectra, (d) Mo 3d spectra. (e) Normalized Fe K-edge XANES spectrum of FeMoCCN and reference materials, and (f) related valence states obtained from Fe K-edge. (g) The k^3-weighted EXAFS of samples, and (h) corresponding fitting curve of R space in XANES. (i) Mo K-edge XANES spectra of different samples, and (j) related valence states obtained from Mo K-edge. (k) EXAFS curves of Mo. (l) EXAFS fitting curve of FeMoCCN. (m-p) WT-EXAFS plots of the Fe and Mo edge.

n, Figs. S9 and S10 in Supporting information) [24]. In the XANES spectra of Mo in FeMoCCN, the curve is closer to MoO_2, and the valence state of Mo is obtained to be 4.1 through linear relationship, which means that Mo mainly exists in the +4 state, consistent with the experimental results in XPS (Figs. 1i and j) [25]. Additionally, according to the EXAFS and the fitting curve of the k-edge, a separate Mo-N shell is seen at approximately 1.3 Å, indicating the presence of Mo-N bonds in the structure (Figs. 1k and l) [26]. This result is further verified by WT for FeMoCCN (Figs. 1o and p). Notably, the novel peaks in the R-space EXAFS spectra of Fe and Mo can be attributed to Fe-Mo at ~2.5 Å, and the fitting curves further confirm the optimal configuration Fe-Mo (Figs. 1g and k) [27], implying the strong connection of Fe and Mo atoms in the catalyst, which is beneficial for the electronic structure regulation and surface adsorption/activation capacity enhancement for degradation.

Tetracycline hydrochloride (TCH) degradation under various conditions is investigated and shown in Fig. 2. As displayed in Figs. 2a and b, the co-existence of Fe and Mo might accelerate degradation as compared to CCN, both under light irradiation and with PMS addition, with a kinetic constant of 0.0112 min^{-1} and 0.0407 min^{-1}, respectively, attributed to the co-catalytic capacity of Mo and the catalytic role of Fe upon light irradiation or for PMS activation. The degradation efficiency of CCN generated by the addition of carbon rings is 25% higher than that of the original carbon nitride (CN) (Fig. S11 in Supporting information), confirming that the C=O on the surface of CCN is conducive to the adsorption and activation of PMS to generate $SO_4^{\bullet-}$ and $^{\bullet}OH$, while the electron coupling of sp^2 bonding structure in the carbon rings accelerates the transfer of electrons [9]. Of note, an optimum performance was observed with a metal loading content of 5%, demonstrating the feasibility and universality of such a preparation strategy for the practical application. Inspired by this situation, the pollutant removal efficiency and the synergistic effect were further explored and discussed in the light-driven PMS system (Fig. 2c). Intriguingly, the degradation efficiency for CCN, MoCCN, FeCCN, $FeMoCCN_{0.25}$, $FeMoCCN_1$, and $FeMoCCN_4$ are 38.8%, 46.8%, 77.2%, 80.9%, 92.1%, and 88.3% within 30 min, respectively, with corresponding reaction rate constants of 0.0168, 0.0219, 0.0517, 0.0526, 0.1178, and 0.0919 min^{-1}, in which $FeMoCCN_1$ performed compelling activity for TCH. Upon irradiation, PMS act as an electron acceptor to capture electrons, thus suppressing charge recombination and enhancing performance [28]. Of note, it should be mentioned that PMS might decompose itself for the production additional non-radical species like SO_4^{2-}, further enhancing degradation of antibiotics, which is also confirmed by the removal efficiency of 25% in the photo-synergistic PMS reaction without catalyst (Fig. S12 in Supporting information) [29,30]. Furthermore, the control experiments in dark are exhibited in Fig. 2d, and an adsorption-desorption equilibrium within 30 min was observed with no obvious effect. Overall, for the three systems of light irradiation, PMS, and light-driven PMS, the introduction of an equivalent proportion of Mo to FeCCN results in an increase in the rate constants by 0.0098, 0.0223, and 0.0858 min^{-1}, respectively, indicating promoted capacity of catalyst in PMS activation and pollutants degradation (Fig. 2e). Moreover, the reaction rate constant of $FeMoCCN_1$ in the light-driven PMS system is significantly higher than that under light irradiation

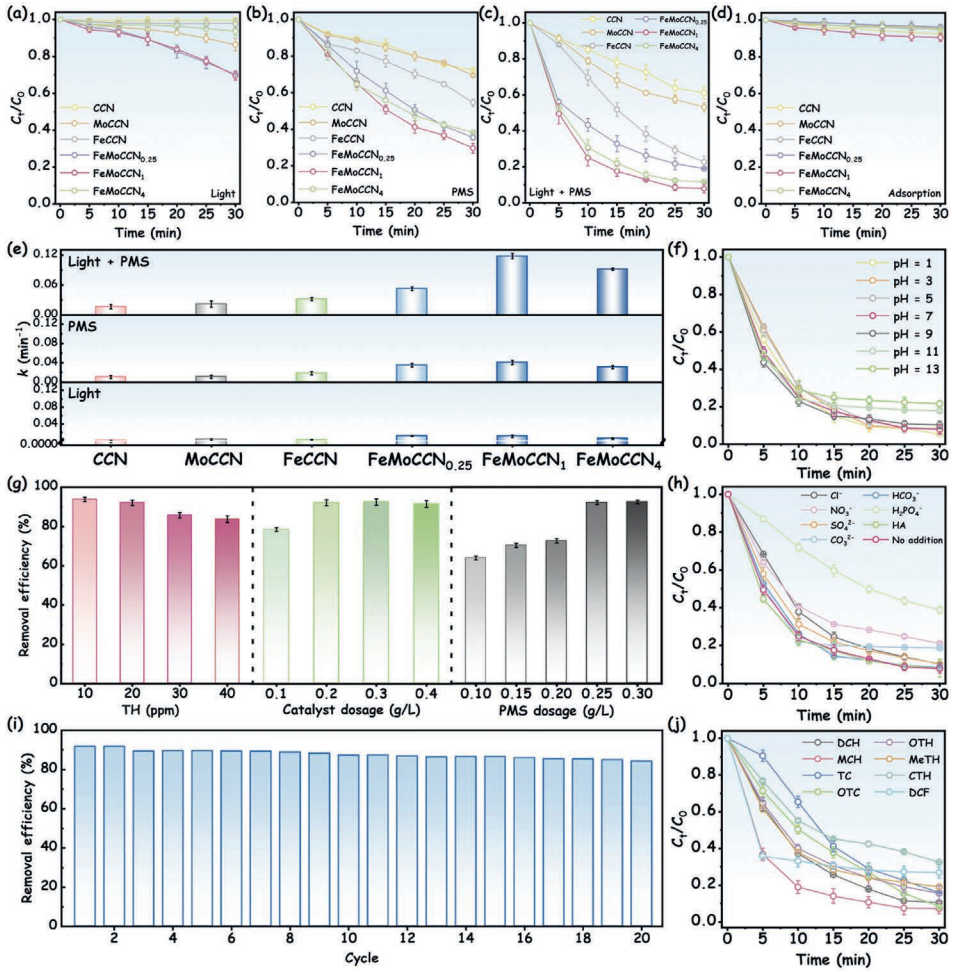


Fig. 2. TCH degradation by different catalysts: (a) under light irradiation, (b) with PMS addition, (c) with PMS addition under light irradiation, (d) dark adsorption, (e) corresponding reaction rate constants. The removal efficiency of TCH over $FeMoCCN_1$ (f) under varying pH conditions, (g) with diverse TCH, catalyst and PMS addition, (h) with the existence of additional anions. (i) Stability test of $FeMoCCN_1$, and (j) removal efficiency of $FeMoCCN_1$ for pollutants. DCH: doxycycline hydrochloride; MCH: minocycline hydrochloride; TC: tetracycline; OTC: oxytetracycline; OTH: oxytetracycline hydrochloride; MeTH: methacycline hydrochloride; CTH: chlortetracycline hydrochloride; DCF: diclofenac.

alone ($0.0112\ min^{-1}$) and PMS alone ($0.0407\ min^{-1}$), further highlighting the indispensable nature of both light and PMS in such a Fenton-like reaction.

Considering the complex environment in practical applications, several environmental parameters including pH, TCH concentration, catalyst and PMS addition amount have been systematically investigated over $FeMoCCN_1$ (Figs. 2f and g). As signified in Fig. 2f, no obvious decrease was observed within the pH range of 1–9, demonstrating the stability in both acidic and neutral environments. Intriguingly, the slight decline under strong alkaline conditions like 11 and 13 might be ascribed to the tendency of Fe^{2+} or Fe^{3+} to combine with OH^- to form complexes. As exhibited in Fig. 2g, the overall removal efficiency of systems with different TCH concentrations all exceeds 80 %, while the degradation capacity of the system slightly decreases along with the increased TCH concentration, owing to the fact that the active sites of the catalyst reach the saturation at higher TCH concentrations and the intermediates decomposed from TCH might also compete for the active sites [31]. When the concentration of antibiotic is 20 ppm, the kinetic constant increases significantly, and its value is $0.011\ min^{-1}$, higher than that in the solution concentration of 10 ppm. Besides, the effect of the catalyst addition content is also investigated in a range from 0.1 g/L to 0.4 g/L, with a reaction constant of 0.0667, 0.1178, 0.1179, and $0.12\ min^{-1}$, respectively. Of note, the pollutant removal efficiency tends to level off after reaching 0.2 g/L. Furthermore, concerning the concentration of PMS, when PMS content is 0.25 g/L, there is a significant increase in degradation efficiency, which is 28.3 % higher than that at a concentration of 0.10 g/L, and the reaction constant maintains a good value. Taking into account the green cycling, degradation performance, and cost for practical application, the concentrations of TCH, catalyst, and PMS for further investigation are set to 20 ppm, 0.2 g/L, and 0.25 g/L, respectively.

Moreover, the impact of various anions (Cl^-, NO_3^-, SO_4^{2-}, *etc.*) existing in actual wastewater was evaluated to ensure practicality of the prepared system (Fig. 2h and Text S4 in Supporting information). Obviously, HCO_3^- and HA have essentially no effect on the activity of the reaction. Interestingly, NO_3^- and Cl^- have a slight inhibitory effect, attributed to NO_3^- and Cl^- can act as scavengers for $^{\bullet}OH$, subsequently generating $ClOH^{\bullet-}$ and $NO_3^{\bullet-}$, which are less reactive, thereby reducing the degradation performance [29]. Meanwhile, SO_4^{2-} is a substance that is easily reduced by electrons, competing with reactive oxygen species in the system ($^{\bullet}OH$, $^{\bullet}O_2^-$) to react and form SO_3^{2-}, thus hindering the reaction. Solution containing CO_3^{2-} exhibits a strong alkaline property, which hinders the circulation of Fe^{3+}/Fe^{2+} and reduces the degradation. Of note, the degradation rate decreases obviously with $H_2PO_4^-$ addition, attributed to the formation of phosphate salts with metal in the catalyst, which might suppress the activation function of the catalyst on PMS. Additionally, the influence of metal ions on

the FeMoCCN/light/PMS system was investigated. It could be found that, after the addition of Na^+, Mg^{2+}, K^+, Ca^{2+}, the degradation efficiency still reached 90%, 85.6%, 89.5% and 83.7%, respectively (Fig. S13 in Supporting information). Overall, it can be concluded that the addition of these anions does not exert a noticeable obstructive effect on the reaction, demonstrating the sustainable capacity of such a system in practical applications.

Subsequently, long-term stability test only a slight decrease of 7.5% within 20 cycles was further carried out, owing to the loss of catalyst during recycling process, with unchanged characteristic peaks in XRD pattern after reaction (Fig. 2i and Fig. S14 in Supporting information). Observed from the XPS spectra of catalyst after reaction, the Fe $2p_{3/2}$ peak ratio decreases from 59.7% to 47.8%, while Fe $2p_{1/2}$ ratio increases from 20.5% to 24.6%, ultimately realizing a reduced Fe^{2+}/Fe^{3+} ratio by 0.97. In addition, the ratio of Mo^{4+}/Mo^{6+} decreases from 1.72 to 1.60 after reaction, confirming that Mo^{4+} might promote the regeneration of Fe^{2+} and is involved in the PMS activation process (Fig. S15 in Supporting information). Furthermore, inductively coupled plasma mass spectrometry (ICP-MS) reveal that the leaching concentrations of Fe and Mo are 0.73 mg/L and 0.70 mg/L, respectively, which are significantly lower than some regions of China standards for metal emissions (2 mg/L), reflecting the environmental adaptability and stability of the catalyst. In addition, the catalytic capacity of the sample was further detected over some other antibiotics with varying electron-donating/electron-withdrawing capacities (Fig. 2j). Intriguingly, the degradation efficiencies of DCH, MCH, TC, OTC, OTH, MeTH, CTH, DCF are 90%, 93%, 85%, 92%, 85%, 81%, 68% and 75%, respectively, together with removal efficiency of 99.7% and 99% for RhB and AO7, confirming the purification capacity of such a catalytic system for a wide range of organic pollutants (Fig. S16 in Supporting information).

In order to identify the possible existing reaction species in the whole process, a series of free radical trapping experiments have been conducted to investigate the contribution of different reactive oxygen species (ROS) for TCH degradation. In this case, *tert*–butanol (*t*-BuOH), chloroform ($CHCl_3$), furfuryl alcohol (FFA) and ethanol (EtOH) are utilized to capture $^{\bullet}OH$, $^{\bullet}O_2^-$, $^1O_2$ and h^+, respectively. Meanwhile, methanol (MeOH) is used to remove $^{\bullet}OH$, and $SO_4^{\bullet-}$ [6]. Of note, oxalate was adopted to suppress the formation of high-valent iron-oxo, thus affecting the degradation efficiency of TCH. In the FeMoCCN/light system, the strongest inhibitory effect with a degradation rate of 1.79% can be observed with the addition of EtOH, indicating that photo-generated holes play a dominant position for pollutants removal (Fig. 3a). In the FeMoCCN/PMS system, $^1O_2$ emerged as the primary reactive species since the degradation rate of TCH dropped to 23.76% with the addition of FFA, and the role of high-valent iron-oxo was detected while the degradation efficiency decreased to 30.71% (Fig. 3b).

Fascinatingly, $^1O_2$ remains the primary reactive species in the FeMoCCN/light/PMS system, with its degradation rate is 45.3%, possibly owing to the sustainable valence cycling of Fe and Mo, as well as the synergistic effects of light and PMS with ideal electrons transfer (Fig. 3c) [32]. Notwithstanding, comparative experiments conducted under air, nitrogen, and argon atmospheres are carried out and no significant decline in activity can be observed, validating that $^1O_2$ is primarily obtained by the activation of PMS over FeMoCCN (Fig. S17 in Supporting information), which is beneficial for further practical application [33]. The addition of *t*-BuOH and $CHCl_3$ both lead to a slight decrease in the degradation, showing that $^{\bullet}OH$ and $^{\bullet}O_2^-$ also participate in the reaction. Meanwhile, the significantly decreased activity with the introduction of oxalate signified that high-valent iron-oxo also plays an indispensable role in the system, capable of forming complexes with pollutants to achieve removal purposes [34].

To further explore the effect of Mo incorporation through bimetallic-doping modulation over the system, the existing active species in the presence of CCN, MoCCN, and FeCCN are carried out as comparison. In the CCN/light/PMS system, *t*-BuOH, $CHCl_3$, and oxalate have no significant inhibitory effect, while MeOH has a certain inhibitory effect, indicating that $SO_4^{\bullet-}$ is also involved in the reaction (Fig. 3d). Notably, the degradation effects of *t*-BuOH and MeOH in the MoCCN/light/PMS reaction system are similar, suggesting that $SO_4^{\bullet-}$ hardly participate in the reaction (Fig. 3e). At the same time, the introduction of Mo enhances the role of $^{\bullet}O_2^-$, and FFA reduces the degradation efficiency of the reaction by 5.6%, mainly attributed to the multivalent state of Mo could promote electron transfer, enabling it to participate in various redox processes [35]. Upon introducing Fe into CCN, the role of high-valent iron-oxo seems vital while the contribution of $SO_4^{\bullet-}$ reduces, owing to high-valent iron-oxo makes electrons more inclined to be transferred to it (Fig. 3f) [36]. Additionally, high-valent iron may also compete with sulfate radicals, thereby reducing their contribution. Interestingly, when Mo is introduced around Fe atoms, the selectivity for $^1O_2$ formation is promoted, ascribed to desirable metal redox cycling *via* synergistic Fe/Mo catalytic-co-catalytic interactions and accelerated electrons transfer and PMS activation [37].

Following this, electron spin resonance (ESR) further verifies the formation of reactive species during the reaction. As exhibited in Figs. 3g-i, there are basically no significant signals under dark condition. In contrast, TEMP-$^1O_2$, DMPO-$^{\bullet}O_2^-$, and DMPO-$^{\bullet}OH$ appear upon irradiation, proving that they all play certain roles in photocatalysis. However, unchanged peak intensities can be observed after being irradiated for 10 min, which is consistent with its weak degradation performance. Following this, PMS was further added into such a system for comparison. Excitingly, the peak intensities of $^1O_2$, $^{\bullet}O_2^-$, and $^{\bullet}OH$ significantly increased, and a new characteristic signal of $SO_4^{\bullet-}$ appeared in Fig. 3i ($\alpha_N = 13.2$ G, $\alpha_H = 9.6$ G, $\alpha_H = 1.48$ G, $\alpha_H = 0.78$ G) [13,38], manifesting the strengthened active species intensity owing to the synergistic effect of PMS activation and photocatalysis, which are consistent with the scavenger experiments. Moreover, in-deep investigation is carried out using PMSO as the probe to quantify the contribution of high-valent iron-oxo species during the reaction, since PMSO can be selectively oxidized by high-valent iron-oxo through an oxygen atom transfer (OAT) reaction to form $PMSO_2$, which is commonly adopted to distinguish the role of high-valent iron-oxo and free radicals in the reaction [39]. As shown in Fig. S18 (Supporting information), the concentration of PMSO decreases by 0.29 mmol/L after 30 min, while the amount of $PMSO_2$ generated is 0.24 mmol/L. The conversion rate of $PMSO_2$ is consistently maintained above 80%, further verifying the role of high-valent iron-oxo ($\equiv Fe^{IV}=O$ or $\equiv Fe^{V}=O$) in the oxidation process.

The potential reaction mechanism is revealed through DFT calculations, with adsorption energy (E_{ads}) comparison for PMS and TCH molecules (Figs. 4a-h). It can be observed that PMS preferentially adsorbs onto the triazine ring of carbon nitride rather than the carbon ring, owing to the stronger electron-withdrawing properties of the latter (Figs. S19a and b in Supporting information), which can motivate electrons transportation towards the carbon ring under light irradiation [40]. The E_{ads} value of single-metal-doped MoCCN (−5.901 eV) is more negative than that of FeCCN (−5.979 eV), indicating that PMS is more likely to adsorb on FeCCN, which is beneficial for the enhancement of the activity (Figs. S19c and d in Supporting information). Furthermore, the E_{ads} values of PMS on the Mo and Fe sites of FeMoCCN are calculated, revealing that the Fe sites (−8.429 eV) exhibit a stronger affinity for PMS adsorption compared to the Mo sites (−6.129 eV). Additionally, the preferential adsorption of TCH on FeMoCCN also implies the regulated active sites and electronic structure are vital for the enhanced

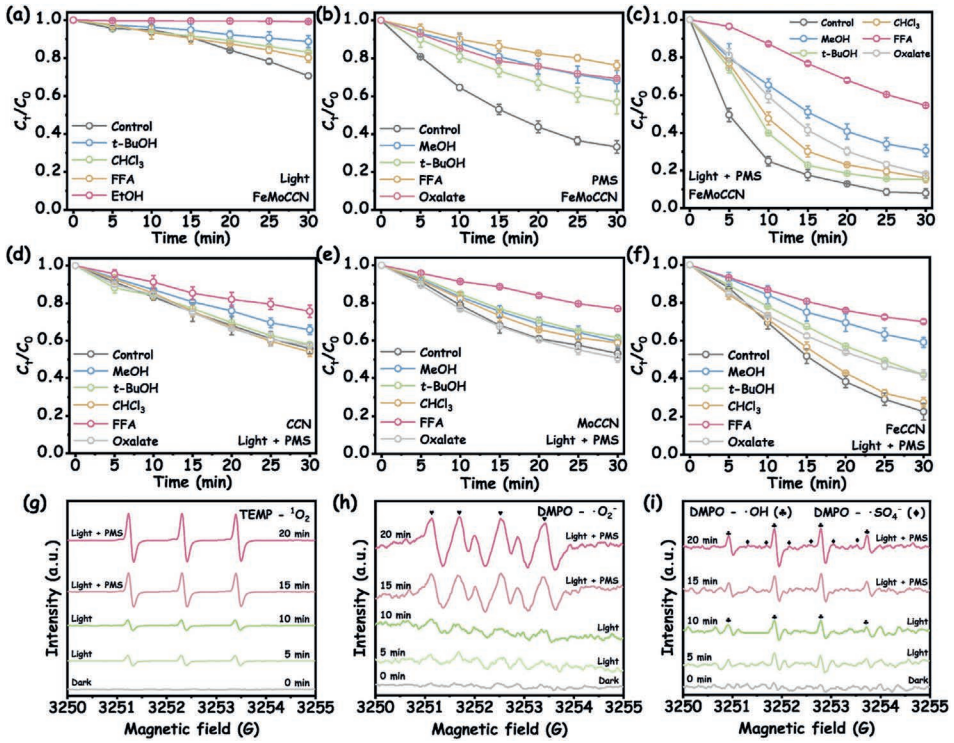


Fig. 3. TCH degradation with different free radical scavengers (a) in FeMoCCN under light conditions, (b) in FeMoCCN with the addition of PMS, (c) in FeMoCCN with PMS addition under light irradiation, (d) in CCN with PMS addition under light irradiation, (e) in MoCCN with PMS addition under light irradiation, (f) in FeCCN with PMS addition under light irradiation. ESR spectrum of (g) TEMP-$^1O_2$, (h) DMPO-$^{\bullet}O_2^-$, (i) DMPO-$^{\bullet}OH$ and DMPO-$^{\bullet}SO_4^-$.

catalytic performance (Figs. 4e-h, Fig. S20 in Supporting information).

To elucidate the influence of Mo incorporation on the electronic structure of Fe active sites, projected density of state (PDOS) and crystal orbital Hamilton population (COHP) are calculated (Figs. 4i-l, Fig. S21 in Supporting information). The positive and negative values of -COHP denote the contributions of bonding and anti-bonding orbitals, respectively [41]. Notably, theoretical analysis reveals a significantly higher bonding orbital contribution in FeMoCCN (3.32 eV) compared to FeCCN (2.78 eV). This enhancement stems from bimetallic interactions and electron redistribution effects, which strengthen interatomic attractive forces and consequently stabilize the Fe-O bond [42]. Moreover, the higher -ICOHP value of FeMoCCN (2.41 eV) confirms the increased Fe-O overlap upon TCH adsorption, indicating stronger covalent bonding character [43]. This observation confirms that Mo incorporation increases Fe-O covalency and strengthens surface adsorption, thereby facilitating electron transfer and promoting PMS activation.

Additionally, upon the detection of Fe^{2+} and Fe^{3+} contents during the reaction process, it is observed that the concentration of Fe^{2+} in FeCCN is 0.9 mg/L, while FeMoCCN generates Fe^{2+} that is about 6 times higher than that of FeCCN, nearly 5.7 mg/L, further confirming that the addition of Mo enhances the utilization efficiency of Fe and promotes the valence cycling of Fe (Fig. S22 in Supporting information). Besides, since FeMoCCN shows the smallest impedance curve radius and highest photocurrent density under light irradiation, the strengthened surface electrons migration and separation *via* bimetallic-doping modulation is further confirmed (Figs. 4m-o). Besides, a significant improvement can be observed for FeMoCCN as compared to other catalysts in linear scanning voltammetry (LSV) spectra, demonstrating the promoted photo-response capability and electrons transfer upon Mo introduction (Fig. 4p).

In order to gain a deeper understanding of the degradation effect of the system, the existing organic intermediates during the process have been analyzed using high performance liquid chromatography-mass spectrometry (HPLC-MS), and three possible degradation pathways have been proposed including steps like N-demethylation, dehydration, hydroxylation, and deamination (Fig. 5). Firstly, HCl in TCH (**P1**) easily dissociates into ions in water and tetracycline (TC) is formed (**P2**). Tetracycline is further attacked by reactive free radicals and non-radical species in the reaction system, breaking down into smaller molecules. In Pathway I, the dimethylamino group (C_4), an active reactive site, is first attacked by $^{\bullet}O_2^-$, losing a methyl group to form P3, which is then further *N*-demethylated to yield **P4**. Subsequently, $^1O_2$ attacks **P3** to remove its hydroxyl group and transform it into **P5**. It is noteworthy that the aromatic ring can be opened by reactive substances to form **P6**, and then undergo oxidative cleavage and intramolecular rearrangement to gain **P7**-**P9** [44]. In reaction pathway II, TC is converted to P10 through hydroxylation. The C–N bond in the -$N(CH_3)_2$ group of **P10** has a low bond dissociation energy, making it more susceptible to attack and demethylation by reactive species. Consequently, under the influence of reactive oxygen species such as $SO_4^{\bullet-}$, $^1O_2$, and $^{\bullet}O_2^-$, **P2** loses two methyl groups to form **P11**. Following this, the reactive sites in **P11**, including the amide bond (C_2) and the dimethylamino group (C_4), are oxidized upon attack to yield **P12**. **P12** then undergoes oxidative cleavage and dehydroxylation to produce the smaller molecules **P13**-**P16** [45]. The intermediate products generated above are eventually further attacked and decomposed into smaller molecules (**P17**-**P19**). Additionally, in Pathway III, TC undergoes dehydration under the action of $^1O_2$ to obtain **P20**, and then another reactive site - the *ortho* position of the phenolic hydroxyl group (C_9) is attacked, leading to ring-opening to form **P21**. **P22** is obtained through dehydroxylation, deamidation, *N*-demethylation, and oxidative ring-opening of **P21**, and **P22** is

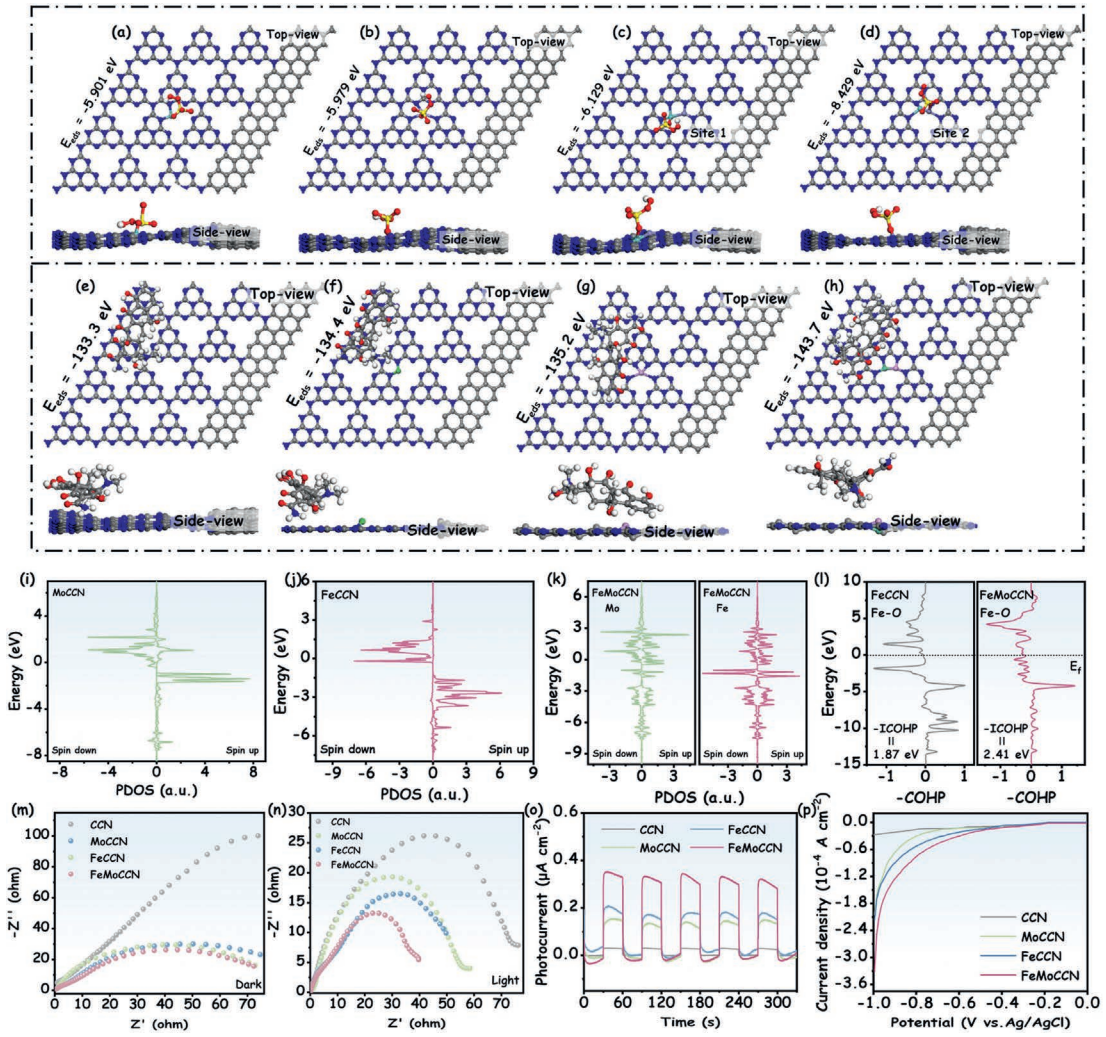


Fig. 4. Theoretical configuration of PMS adsorption on MoCCN (a) and FeCCN (b). Adsorption energy of PMS on Mo sites in FeMoCCN (c) and on Fe sites in FeMoCCN (d). Top view and side view of TCH optimal adsorption energy calculation configuration for (e) CCN, (f) MoCCN, (g) FeCCN, (h) FeMoCCN. Projected density of state of (i) MoCCN, (j) FeCCN, (k) FeMoCCN. (l) COHP analysis of different catalysts upon the adsorption of TCH. Electrochemical impedance spectra (EIS) of catalysts under (m) dark conditions, (n) light conditions. (o) Photocurrent response curves and (p) LSV curves of catalysts. Elements: gray (C), blue (N), white (H), red (O), green (Mo), purple (Fe).

further oxidatively cleaved to yield small molecules **P23**-**P24** (Figs. S23 and S24 in Supporting information).

Using diclofenac as the target, its degradation involves dechlorination, decarboxylation, hydroxylation, dehydrogenation, addition, and C–N bond cleavage (Fig. 5, Figs. S24 and S25 in Supporting information) [46,47]. In route I, **P26** was obtained through decarboxylation and dehydrogenation reactions. Subsequently, C_{11} is further attacked and undergoes hydroxylation while the pollutant molecule undergoes dehydrogenation to form **P27**. Differently, in route II, where C_{14} first experiences decarboxylation to form **P28**, and then is hydroxylated to produce **P29**. Additionally, the C_3 position of DCF is also relatively reactive and susceptible to attack. Besides, in route III, hydroxylation yields **P30**, which increases the electron cloud density on the benzene ring and enhances the tendency for further hydroxylation later on. As a result, **P30** is further attacked to generate the dihydroxy product **P31**, followed by C–N bond cleavage to obtain **P32**. Meanwhile, DCF might also undergo cyclization to form **P33** in route IV. Finally, these intermediate products are further oxidized and decomposed into smaller molecules (**P34**-**P37**).

$$FeMoCCN + h\nu \rightarrow e^- + h^+ \quad (1)$$

$$HSO_5^- \rightarrow SO_5^{\bullet-} + H^+ + e^- \quad (2)$$

$$SO_5^{\bullet-} + SO_5^{\bullet-} \rightarrow S_2O_8^{2-}/2SO_4^{2-} + {}^1O_2 \quad (3)$$

$$Fe^{2+}/Mo^{4+} + HSO_5^- \rightarrow Fe^{3+}/Mo^{6+} + SO_4^{\bullet-} + {}^{\bullet}OH \quad (4)$$

$$Fe^{3+}/Mo^{6+} + HSO_5^- \rightarrow Fe^{2+}/Mo^{4+} + SO_5^{\bullet-} + H^+ \quad (5)$$

$$Fe^{3+}/Mo^{4+} \rightarrow Fe^{2+}/Mo^{6+} \quad (6)$$

$$Fe(III) + HSO_5^- \rightarrow \equiv Fe^{IV}{=}O\ /\equiv Fe^{V}{=}O + SO_4^{2-} \quad (7)$$

$$\equiv Fe^{IV}{=}O\ /\equiv Fe^{V}{=}O + TCH \rightarrow Fe(III) + products \quad (8)$$

$$({}^1O_2,\ SO_4^{\bullet-},\ high\ iron\text{-}oxo\ldots) + TCH \rightarrow small\ molecules \quad (9)$$

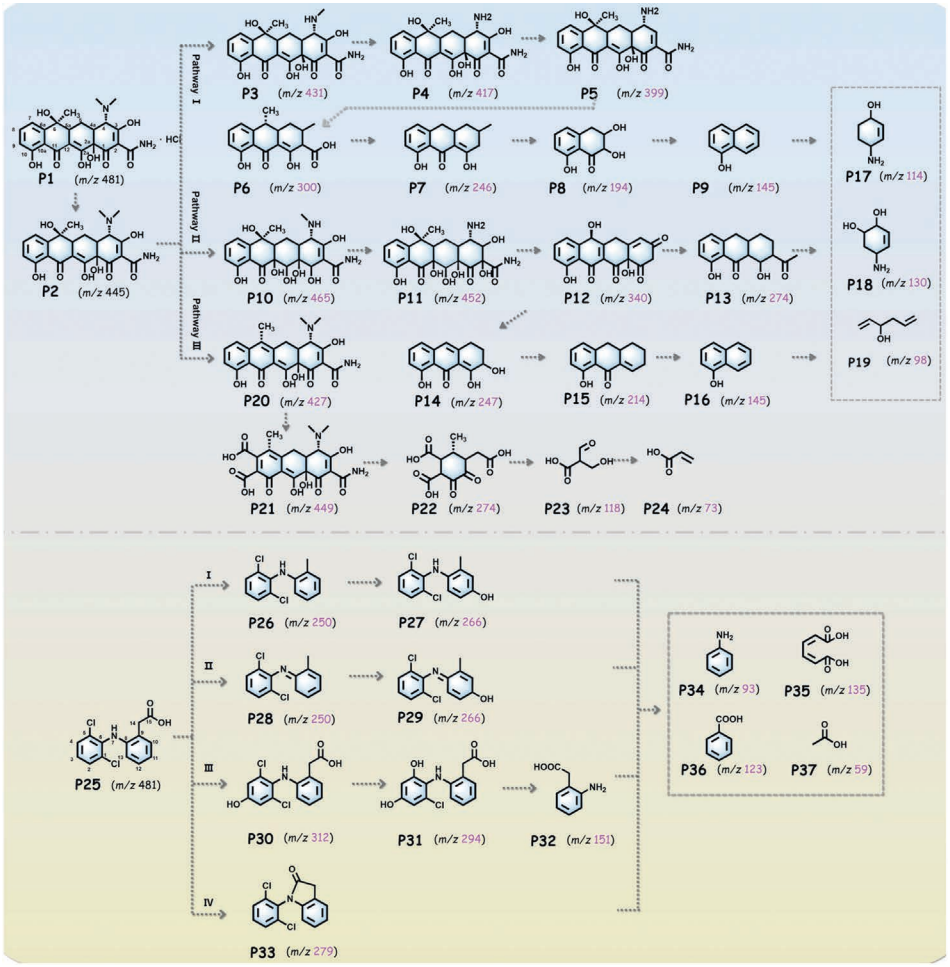


Fig. 5. Possible degradation pathways of TCH and DCF using FeMoCCN.

Based on the analysis of reaction active species and data results, we have proposed a possible degradation mechanism. Upon photo-excitation, electrons (e^-) and holes (h^+) can be generated in FeMoCCN upon irradiation (Eq. 1). Following this, h^+ react with HSO_5^- in PMS to produce $SO_5^{\bullet-}$, which then continuously reacts to generate non-radical $^1O_2$ (Eqs. 2 and 3). It is noteworthy that through the newly formed bond of Fe-Mo, the transition metal redox pair can activate PMS to produce reactive oxygen radicals ($^\bullet$OH, $SO_4^{\bullet-}$, and $SO_5^{\bullet-}$) through Fe^{2+}/Fe^{3+}, Mo^{6+}/Mo^{4+}, Fe^{3+}/Mo^{4+} (Eqs. 4 and 5). Simultaneously, light irradiation accelerates the redox reactions of the metal-pairs, thereby promoting their valence cycling (Eq. 6) [48]. Additionally, Fe(III) can coordinate with PMS to form an intermediate complex $[Fe(III)OOSO_3]^+$. Subsequently, heterolysis of the O–O bond in the intermediate leads to the formation of high-valent iron-oxo active species ($\equiv Fe^{IV}=O/\equiv Fe^{V}=O$), which then react with TCH, producing Fe(III) for the next cycling (Eqs. 7 and 8) [34]. Ultimately, the radicals like $^\bullet$OH and non-radicals including $^1O_2$ high valent iron-oxo, oxidize TCH to form a series of small molecule substances (Eq. 9).

In summary, enlarged Fe-O covalency enabled by Mo doping, with Fe-N_4 as active sites and tight Fe-Mo bonds as electron transfer bridge, has been developed for water remediation. Satisfied efficiency for antibiotic wastewater cleanup and ideal circulation of transition metallic redox couples is detected, with TCH removal efficiency of 92.1 % within 30 min in a neutral environment, together with long-term stability. Interestingly, the strengthened Fe-O covalency *via* Mo incorporation is confirmed, thereby benefiting the electrons transfer for PMS activation and further degradation. Accordingly, the sustainable metal redox cycling enabled from synergistic Fe/Mo catalytic-co-catalytic interactions, enhanced bonding orbital overlap, and optimized surface adsorption capacity, all account for the promoted removal efficiency of FeMoCCN in Fenton-like reactions, providing a deep insight into the synergistic effect of light irradiation and oxidant activation as well as bimetallic-doping modulation for wastewater cleanup.

CRediT authorship contribution statement

Jiaqi Wu: Writing – original draft, Investigation. **Fengze Zhuang:** Resources, Formal analysis. **Yuqiu Xie:** Formal analysis. **Yue Chen:** Formal analysis. **Xiaofei Zeng:** Formal analysis. **Liang Chen:** Methodology, Software. **Bocheng Qiu:** Writing – original draft, Methodology. **Qiaohong Zhu:** Writing – review & editing, Investigation, Formal analysis, Data curation, Conceptualization. **Mingyang Xing:** Writing – review & editing, Supervision, Funding acquisition, Formal analysis, Data curation.

Declaration of competing interest

The authors declare that they have no known competing financial interests or personal relationships that could have appeared to influence the work reported in this paper.

Acknowledgments

The study was financially supported by National Key R&D Program of China (No. 2024YFC3712704), National Natural Sci-

ence Foundation of China (Nos. 22521201, 22325602, 22176060, 22406047, 22171064, 22302095), the Natural Science Foundation of Zhejiang Province (No. LQ23B030003), the HZNU scientific research and innovation team project (No. TD2025017).

Supplementary materials

Supplementary material associated with this article can be found, in the online version, at doi:10.1016/j.cclet.2026.112508.

References

[1] S. Xu, X. Mi, P. Wang, et al., Adv. Funct. Mater. 33 (2023) 2308204.
[2] Z. Chen, J. Li, B. Yang, et al., Chin. J. Chem. 42 (2024) 2563–2571.
[3] J. Yang, S. Wang, X. Luo, et al., Chin. Chem. Lett. 36 (2025) 110996.
[4] Z. Liu, R. Su, F. Xu, et al., Adv. Mater. 36 (2024) 2311869.
[5] Y. Pan, J. Cao, M. Xing, et al., ACS ES&T Eng. 4 (2024) 19–46.
[6] J. Zhen, J. Sun, X. Xu, et al., Angew. Chem. Int. Ed. 63 (2024) e202402669.
[7] H. Dai, W. Zhou, W. Wang, et al., J. Hazard. Mater. 426 (2022) 127784.
[8] H. Li, C. Shan, B. Pan, Environ. Sci. Technol. 52 (2018) 2197–2205.
[9] H. Li, C. Shan, B. Pan, Sci. Total Environ. 675 (2019) 62–72.
[10] A. Wang, M. Du, J. Ni, et al., Nat. Commun. 14 (2023) 6733.
[11] C. Song, Q. Zhan, F. Liu, et al., Angew. Chem. Int. Ed. 61 (2022) e202200406.
[12] X. Zhang, C. Zhou, J. Zhang, et al., Chin. Chem. Lett. 37 (2026) 111630.
[13] H. Shi, Y. He, Y. Li, et al., ACS Catal. 13 (2023) 8973–8986.
[14] Z. Zhao, W. Zhou, D. Lin, et al., Appl. Catal. B: Environ. 309 (2022) 121256.
[15] Z. Chen, F. An, Y. Zhang, et al., Proc. Natl. Acad. Sci. U. S. A. 120 (2023) e2305933120.
[16] F. Chen, X.L. Wu, C. Shi, et al., Adv. Funct. Mater. 31 (2021) 2007877.
[17] Z. Liu, X.Y. Xu, F. Xu, et al., Water Res. 274 (2025) 123147.
[18] M. Cui, K. Cui, X. Liu, et al., J. Hazard. Mater. 418 (2021) 126338.
[19] Y. Liu, W. Miao, Z. Chen, et al., Chem. Eng. J. 496 (2024) 153871.
[20] L. Qin, J. Meng, G. Yang, et al., Appl. Catal. B: Environ. Energy 345 (2024) 123695.
[21] X.D. Yang, Y. Zheng, J. Yang, et al., ACS Catal. 7 (2017) 139–145.
[22] M. Mateen, W.C. Cheong, C. Zheng, et al., Chem. Eng. J. 451 (2023) 138305.
[23] F. Chen, Y.J. Sun, X.T. Huang, et al., Proc. Natl. Acad. Sci. U. S. A. 121 (2024) e2314396121.
[24] Y. Li, J. Wei, N. Cui, et al., Appl. Catal. B: Environ. Energy 358 (2024) 124385.
[25] C. Dong, Z. Wang, C. Yang, et al., Proc. Natl. Acad. Sci. U. S. A. 120 (2023) e2305883120.
[26] Z. Fan, H. Cheng, B. Pang, et al., ACS Appl. Mater. Interfaces 17 (2025) 4804–4812.
[27] R. Li, R. Ma, L.L. Zhang, et al., ACS Nano 19 (2025) 17686–17697.
[28] Q. Ji, K. Du, J. Zhu, et al., Chem. Eng. J. 462 (2023) 142116.
[29] R. Guo, Y. Wang, J. Li, et al., Appl. Catal. B: Environ. 278 (2020) 119297.
[30] K.A. Zhu, X.J. Chen, C.W. Yuan, et al., J. Hazard. Mater. 445 (2023) 130476.
[31] Z. Li, M. Sun, J. Yang, et al., Chem. Eng. J. 446 (2022) 137380.
[32] Z. Zhao, M. Hu, T. Nie, et al., Environ. Sci. Technol. 57 (2023) 4556–4567.
[33] J. Jiang, S. Liu, D. Shi, et al., Water Res. 244 (2023) 120502.
[34] Y. Bao, C. Lian, K. Huang, et al., Angew. Chem. Int. Ed. 61 (2022) e202209542.
[35] M.Y. Lan, Y.H. Li, C.C. Wang, et al., Nat. Commun. 15 (2024) 7208.
[36] Y.S. Zhang, X.J. Chen, X.T. Huang, et al., Water Res. 260 (2024) 121907.
[37] F. Chen, L.L. Liu, J.H. Wu, et al., Adv. Mater. 34 (2022) 2202891.
[38] Y. Jiang, Z. Yang, X. Bi, et al., Chin. Chem. Lett. 35 (2024) 109331.
[39] C. Liu, J. Li, X. He, et al., Proc. Natl. Acad. Sci. U. S. A. 121 (2024) e2322283121.
[40] Z. Mo, J. Di, P. Yan, et al., Small 16 (2020) 2003914.
[41] X. Li, J. Wang, H. Xue, et al., Adv. Funct. Mater. 35 (2025) 2503360.
[42] Y. Huang, Y. Zhao, D. Song, et al., Appl. Catal. B: Environ. Energy 374 (2025) 125377.
[43] Y. Liu, C. Liu, X. Peng, et al., Water Res. 280 (2025) 123477.
[44] B.B. Zhang, C.W. Bai, X.J. Chen, et al., J. Hazard. Mater. 468 (2024) 133816.
[45] J. Wu, Z. Wang, X. Chen, et al., J. Clean. Prod. 446 (2024) 141391.
[46] X. Li, S. Huang, H. Xu, et al., Chin. Chem. Lett. 33 (2022) 1321–1324.
[47] D. Yang, J. Liang, L. Luo, et al., Chin. Chem. Lett. 32 (2021) 2534–2538.
[48] C. Dong, Y. Bao, T. Sheng, et al., Appl. Catal. B: Environ. 286 (2021) 119930.